Article

Pressure Fluctuation Characteristics of a Pump-Turbine in the Hump Area under Different Flow Conditions

Kai Zheng [1], Liu Chen [2], Shaocheng Ren [2], Wei Xiao [3], Yexiang Xiao [4,*], Anant Kumar Rai [5], Guangtai Shi [6] and Zhengkai Hao [6]

1   State Grid Xinyuan Group Co., Ltd., Beijing 100032, China; 13718607707@163.com
2   China Institute of Water Resources and Hydropower Research, Beijing 100048, China; chenliu@iwhr.com (L.C.); euler@iwhr.com (S.R.)
3   Pumped-Storage Technological & Economic Research Institute State Grid Xinyuan Company Ltd., Beijing 100053, China; xiaoweiyh@126.com
4   Department of Energy and Power Engineering, Tsinghua University, Beijing 100084, China
5   Department of Mechanical Engineering, National Institute of Technology Warangal, Warangal 506004, India; anant@nitw.ac.in
6   Laboratory of Fluid Machinery and Engineering, Xihua University, Chengdu 610039, China; sgtaixh@126.com (G.S.); 18635844538@163.com (Z.H.)
*   Correspondence: xiaoyex@mail.tsinghua.edu.cn

Abstract: During the operation of a reversible pump-turbine, a hump area can easily appear under the pump condition, which will greatly affect the performance of a storage unit, with pressure pulsation being the key factor for the stable operation of a pump-turbine. Therefore, in order to explore the pressure pulsation characteristics of each flow component in the hump area, this paper first compared the full characteristics of the model test under different working conditions, and then it analyzed the pressure pulsation characteristics. By analyzing the pressure pulsation characteristics in the unit's flow component under different flow rates in the hump area, the pulsation rule of a pump-turbine running in the hump area was revealed. It was found that the peak-to-peak value of the draft tube in the hump area was the smallest under the optimal flow condition, and the peak-to-peak value increased along the flow direction, with the rotor and stator interaction (RSI) effects being continuously enhanced. When away from the runner basin, the influence of RSI gradually weakened after leaving the runner. No low frequency was found in the optimal traffic. The peak-to-peak value of the low flow condition increased compared with the optimal flow condition, and the distribution was not uniform. The main frequency of the whole basin was relatively complex, indicating that the flow of water was unstable in the condition of partial load, resulting in the hump area during the unit operation. The research results can provide a theoretical reference for improving the stability of pump-turbines.

Keywords: reversible pump-turbine; pump hump area; pressure fluctuation; RSI

1. Introduction

With the progress of society, the world's non-renewable energy sources have been developed and utilized in large quantities. Non-renewable resources are on the verge of exhaustion [1,2]. To deal with this situation, the use of renewable energy sources has increased significantly [3]. However, these renewable energy sources are excessively dependent on natural conditions and cannot provide electricity continuously and stably, which makes the stability of the power grid face great challenges [4]. Reversible pump-turbines are widely used in pumped storage power stations, which can switch safely and stably between power generation conditions and pumping conditions, making pumped storage power stations the first choice to improve the quality of the grid in terms of the current move towards clean energy, as well as in the development of new energy [5,6].

In order to meet the need of the flexible regulation of the power grid, a pump-turbine needs frequent and rapid shutdown, start-up, and conversion between different modes, resulting in many instability problems. To solve these problems, it is the primary task to understand the complex flow and pressure pulsation characteristics under different working conditions [7,8]. The full characteristic curve of a pump-turbine is usually expressed by four-quadrant characteristics. On this basis, five operation modes are defined: turbine, turbine brake, pump, reverse pump, and pump brake. Due to the lack of design of the pump-turbine and the need to meet different operating conditions, the pump-turbine will produce many unstable phenomena during operation, such as the hump characteristics under the pump condition and the 'S' characteristics under the turbine condition [9,10]. When pump-turbines are operating at low flow conditions, a saddle-shaped area appears on the flow head curve, that is, the hump area [11]. At the same time, when some low specific speed pump-turbines are operating under turbine conditions, an area similar to an 'S' shape appears on the curve of unit speed and unit flow, which is called the 'S' characteristic [12]. The hump characteristic and the 'S' characteristic are two characteristics of the pump-turbine that will affect the normal operation of the pump-turbine. At present, many scholars are devoted to the study of the 'S' characteristics [13,14] and hump characteristic areas [15,16], exploring the internal mechanism of pressure pulsation and seeking improvement methods.

Because the diversion channel of the pumped storage power station unit is long, and the water level difference between the upstream and downstream is large, the design of the unit tends to compress the space of the vaneless area. The operating conditions of the pumped storage power station unit are complex and changeable, and the flow pattern of the pump-turbine is more unstable than that of the simple pump and turbine due to the internal structure. Therefore, the pressure pulsation in the vaneless area of the pump-turbine has become one of the main factors affecting the stable operation of the power station. In particular, factors such as rotating stall [17,18], eddy current [19,20], cavitation [21,22], defluidization [23], and incoming flow disturbance [24] are the main reasons for the internal pressure pulsation of the pump-turbine. For example, Hu et al. [25] found that when the working point is close to the design working point of the pump and turbine, the flow is stable, and the pressure pulsation is small. When the working point deviates from the optimal working point, the flow becomes worse, and the vibration phenomenon occurs. Ma et al. [26] found that the pressure pulsation amplitude of the blade through the frequency component showed inhomogeneity at different vertical positions. Guo et al. [27] analyzed the pressure pulsation characteristics of the pump working condition and concluded that the amplitude of the impeller pressure surface was stronger than that of the low-pressure side. E. Vagnoni et al. [28] analyzed the internal flow structure of the model pump-turbine based on the particle image velocimetry (PIV) test and confirmed the existence of an unstable vortex and backflow in the vaneless region. Maruzewski et al. [29] compared the effects of different turbulence models on the internal flow field and pressure pulsation in the vaneless region and found that the SST k-ω model is more accurate in capturing the pressure pulsation of the guide vane wake.

The existence of the hump area causes the pump-turbine to be in an extremely unstable state during operation, which will cause vibration and noise of the unit [30,31]. It can be seen from the above research that the current research on the hump area of the pump-turbine has achieved rich results, and many causes of the hump area have been found. However, there are few studies on the influence of pressure pulsation on the unit under different flow rates in the hump area of the pump-turbine. Therefore, in order to explore the causes of the unstable working conditions of the pump-turbine, this paper studied the pressure fluctuation characteristics of the pump-turbine under different flow rates in the hump area and explored the pressure fluctuation changes in the flow components of the pump-turbine in the hump area.

2. Research Object

2.1. Physical Model

The research physical model of the paper is a reversible pump-turbine, which is shown in Figure 1. The parameters of the pump-turbine are shown in Table 1. In this study, the specific speed of the pump-turbine was about 43.83.
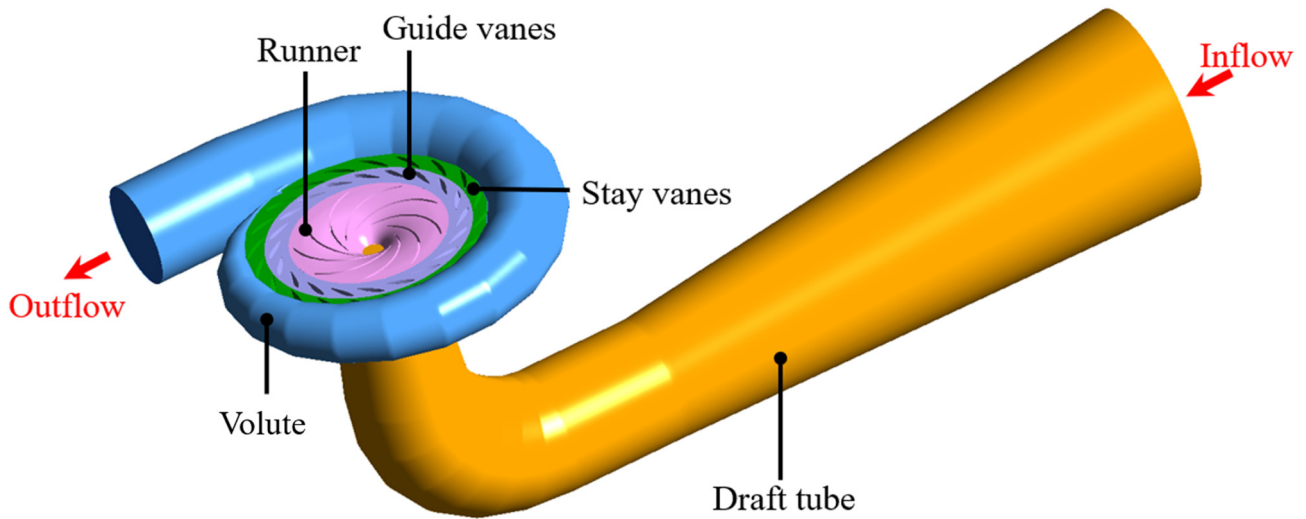

Figure 1. Pump-turbine model diagram.

Table 1. Parameters of the pump-turbine.

Component	Symbol	Value
Runner inlet dia. (mm)	D_1	470
Runner outlet dia. (mm)	D_t	300
Rated rotational speed (rpm)	Nd	1200
Nominal head (m)	H	30
Runner blade number (-)	Z	9
Stay vane number (-)	Z_1	20
Guide vane number (-)	Z_2	20

The parameter conversion formulas running in the pump-turbine are as follows:

$$n_{11} = \frac{nD}{\sqrt{H}} \tag{1}$$

n_{11} is the unit speed, where n is the runner rotational speed, and the unit is rpm; d is the runner nominal diameter, the unit is m; H is the net water head, the unit is m.

$$Q_{11} = \frac{Q}{D^2\sqrt{H}} \tag{2}$$

Q_{11} is the unit flow. Here, Q represents the flow, and the unit is L/s.

$$M_{11} = \frac{M}{D^3\sqrt{H}} \tag{3}$$

M_{11} is the unit torque. M is the torque generated by the rotation of the main shaft of the runner, and the unit is N·m.

2.2. Selection of the Calculation Working Point

The error between the results of the external characteristic parameters of the steady calculation and the test results is still large, and the flow calculation results cannot reflect the real operation process. So as to further study the unsteady flow characteristics in the pump condition and obtain a more realistic actual flow state, two working points were selected for long-term unsteady calculation under the optimal active guide vane opening. The optimal flow condition was 408 L/s(406.8 kg/s), and the partial load condition was 190 L/s (189.4 kg/s).

The 190 L/s flow condition and 408 L/s flow condition, as the two most typical working conditions of the pump-turbine operating under the pump condition, are the most worthy of study. By studying the flow characteristics and pressure pulsation characteristics under the two working conditions, the flow law of the water flow in the pump-turbine will be explored, and the cause of the hump area in the pump-turbine under the pump working condition will be revealed.

2.3. Grid Independence Verification

According to the calculated performance parameters and their comparison with the model test results, a mesh scheme of 2.84 million was finally selected as the computational mesh for flow analysis. The grid division of each channel under this grid density is shown in Figure 2. The volute adopts tetrahedral mesh, and the number of mesh elements is about 600,000. The mesh division is shown in Figure 2a. The stay vane and the guide vane adopt a hexahedral grid basin, and the head and tail of the guide vane are encrypted. The number of grid units is about 290,000 and 340,000, respectively. The grid division is shown in Figure 2b. The runner is the core component in the numerical calculation. When meshing the runner basin, hexahedral grids and high grid density are used, and the head and tail of each blade are encrypted. The number of grid units is 1.2 million, and the meshing situation is shown in Figure 2c. The draft tube basin adopts a hexahedral grid, and the number of grid units is 418,000, as shown in Figure 2d. The aspect ratio and skewness of each component grid are shown in Table 2.

Table 2. Aspect ratio and skewness of each component grid.

Parameter	Aspect Ratio	Skewness
Volute	3.5	0.16
Stay vanes	5.1	0.19
Guide vanes	4.6	0.03
Runner	4.4	0.05
Draft tube	3.7	0.08

Figure 3 shows the distribution of Y + value near the wall surface of the runner area of the reversible pump-turbine. It can be seen that the average value is about 8, and it meets the requirements of the SST k-ω turbulence model for Y+ value [32].

In this study, five grid densities from 1 million to 4 million were calculated. According to the calculation of the optimal performance parameters, a grid scheme of 2.84 million was finally selected for simulation. When the calculated head and efficiency will no longer change with the number of grids, it indicates that the number of grids at this time has reached the calculation requirements, and the number of grids will not affect the accuracy of the calculation. Therefore, it is not necessary to increase the number of grids and avoid wasting computing resources, as shown in Figure 4.
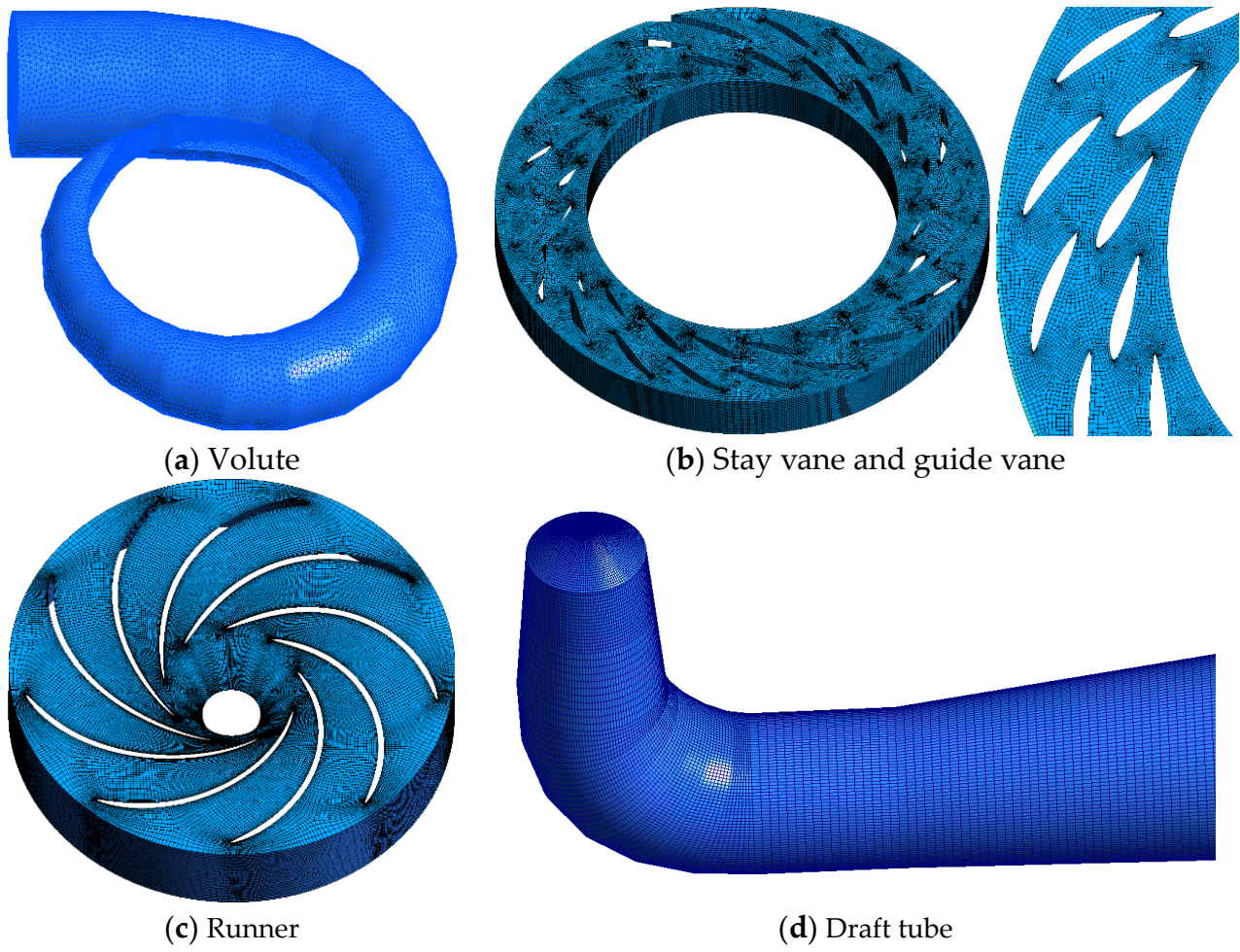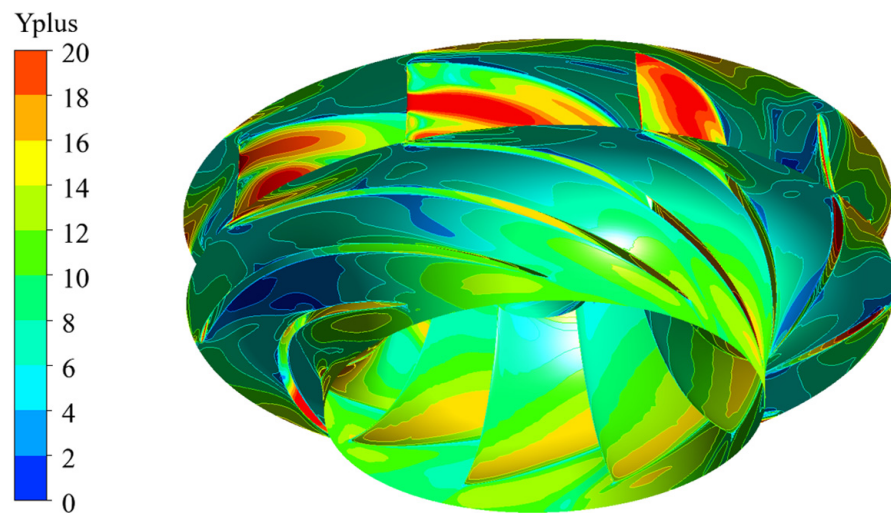
(**a**) Volute

(**b**) Stay vane and guide vane

(**c**) Runner

(**d**) Draft tube

Figure 2. Meshing.

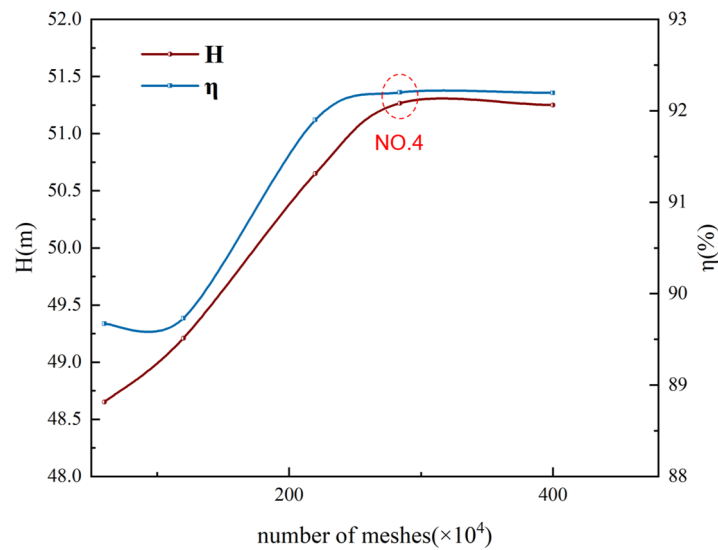**Figure 3.** Y+ value distribution in the runner.

Figure 4. Grid independence verification.

3. Numerical Calculation Settings

3.1. Turbulent Flow Model

The SST k-ω turbulence model that is suitable for low Reynolds number calculation is used in this calculation. This model has the advantages of the SST model and k-ω model, which makes the calculation results more accurate and reliable. The mathematical expression of this model is shown in Formula (4) [33].

$$\frac{\partial}{\partial x_i}(\rho \omega u_i) = \frac{\partial}{\partial x_i}\left(\Gamma_\omega \frac{\partial \omega}{\partial x_j}\right) + G_\omega - Y_\omega + D_\omega + S_\omega \tag{4}$$

In the formula, ω is the turbulent dissipation rate, G_ω is the generation term of the turbulent dissipation rate, Γ_ω is the turbulent dissipation rate effective diffusion coefficient, Y_ω is the dissipation term of the turbulent dissipation rate, D_ω is the orthogonal diffusion term, and S_ω is the source term of the turbulent dissipation rate [33].

3.2. Boundary Condition Setting

For different working conditions in a simulation calculation, mass flow inlet and average pressure outlet should be used. The runner is a rotating part, so the GGI interface should be set between the runner and the guide vane and the draft tube in contact with it. All walls of the flow channel are assumed to be hydraulically smooth, with no-slip boundary conditions applied. And the convergence threshold is set to less than 10^{-5}. The simulation calculation method adopted in this paper can reach convergence after 3000 iterations.

The SST turbulence model is used in the unsteady calculation, and the steady calculation results are taken as the initial conditions of each operating point. The inlet and outlet conditions and the treatment of the interface are the same as those of the steady calculation. For the two dynamic and static interfaces of the guide vane-rotor and the runner-suction pipe, the unsteady calculation adopts the treatment method of the transient rotor stator. Considering the runner rotation speed and the number of blades, the time step is set. The final time step is 1/180 of the runner rotation period, that is, 180 steps are calculated for each rotation period, and the calculation results are saved every two steps. Each working condition calculates 18 rotation cycles of the runner, and the calculation results of the last eight cycles are used to process and analyze the external characteristic parameters.

In the process of the unsteady numerical simulation, the corresponding recording points are set up in the basin to record the change rule of pressure. A total of 72 rotating recording points and 33 static recording points are set up in the whole flow channel. The

72 moving points are located in the nine blade channels of the runner, and eight recording points are arranged in each channel. As shown in Figure 5, the naming rules of the recording points in each channel are similar. For example, the eight moving points in channel 1 are named as rv11-rv18 according to the order of water flow, and the names of the other channels are rv21-rv28, rv31-rv38, rv41-rv48, rv51-rv58, rv61-rv68, rv71-rv78, rv81-rv88, and rv91-rv98.
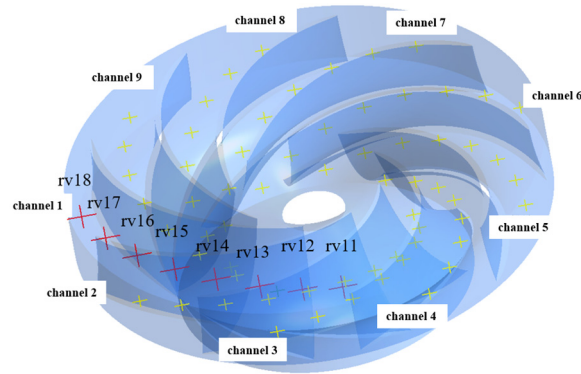

Figure 5. Arrangement of the dynamic pressure recording points in the runner.

The arrangement of the pressure recording points in the static parts is shown in Figure 6. The 33 static recording points are located in the suction pipe, the guide vane, the stay vane, and the volute basin. For the suction pipe basin, a total of 16 recording points are located on four different planes, and four recording points are arranged on each plane, which are evenly distributed around each plane, and they are named dt11-dt44 according to the order of water flow. For the active guide vane basin, a total of eight recording points are arranged on the 0.5-span plane, being located in the leafless area of the inlet and outlet of the active guide vane, and evenly distributed along the circumference. The four points in the leafless area at the inlet of the active guide vane are named gv1-gv4, and the four points in the leafless area at the outlet of the active guide vane are named mv1-mv4; for the fixed guide vane basin, four recording points are arranged at the outlet of the 0.5-span plane, which are evenly distributed along the circumference, and they are named sv1-sv4, respectively. For the volute basin, five recording points are arranged on the 0.5-span plane, located on the outer wall of the volute, named sp1-sp5.
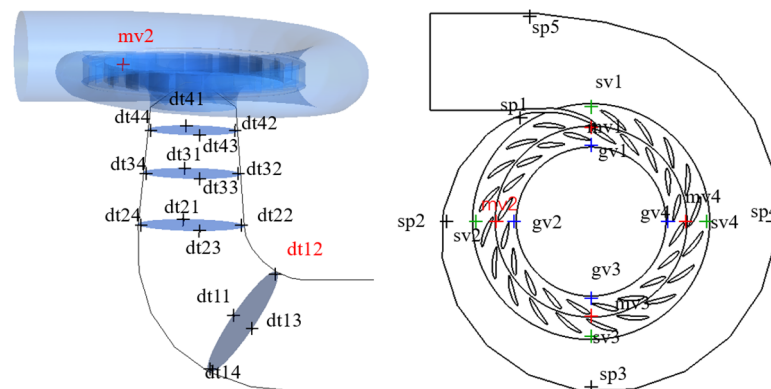

Figure 6. Arrangement of the static pressure recording points in the whole flow channel.

Two pressure sensors are placed in the inner area of the elbow section of the suction tube and the vaneless area between the runner and the guide vane to detect the pressure pulsation. The position of the pressure sensor is marked in red font in Figure 4, being dt12 and mv2 (near the upper wall).

4. Test Verification

Numerical simulations were conducted for a series of operating points of the pump-turbine under different guide vane openings (GVO 46%, 60%, 74%). The unit speed and unit flow characteristics were compared with the model test results at various operating points, as illustrated in Figure 7. The relative errors for head and efficiency were within 0.93% and 3.88%, respectively. Though there were some discrepancies at certain points, the numerical simulation results showed good agreement with the model test data, confirming the accuracy and reliability of the three-dimensional numerical simulation method used in this study [34].
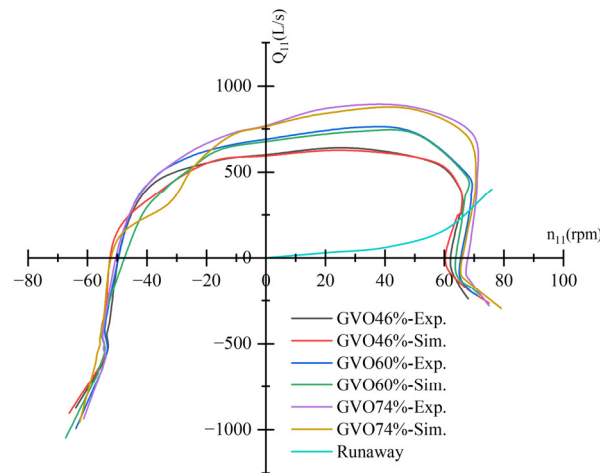

Figure 7. Full characteristic simulation—test results.

5. Analysis of the Results

5.1. Hydraulic Performances of the Pump Hump Area

Figure 8 shows the external characteristic curve of the pump-turbine with a 60% guide vane opening. It can be seen from the figure that within a certain flow range, the Q-H curve had a hump area, that is, the slope of the curve changed from negative to positive. The existence of the hump area made the pump-turbine unable to run stably under the pump condition, resulting in hydraulic loss.
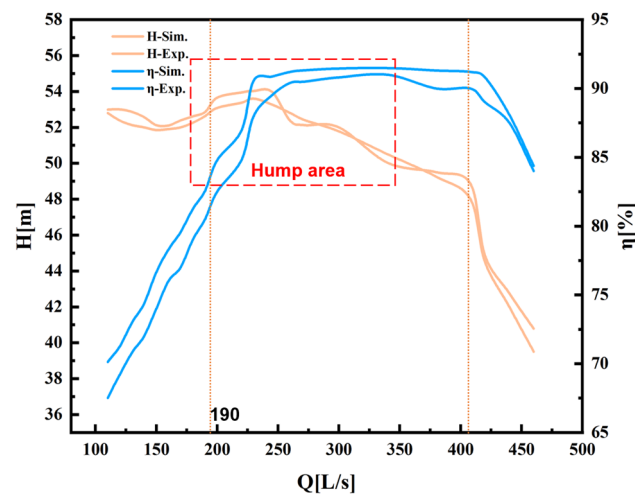

Figure 8. The predicted and experimental *Q-H* and *Q-η* curves.

5.2. Pressure Pulsation Characteristics under Optimal Flow Conditions

Under the optimal working conditions, the mixing amplitude analysis of a total of 72 moving points in 9 channels in the runner domain was first performed. As shown in Figure 9, it can be found that the peak-to-peak variation characteristics were the same in the nine blade channels, and the curves were almost coincident, indicating that the flow of the fluid in the nine channels was similar. In order to simplify the analysis, only eight recording points of channel 1 are analyzed here.
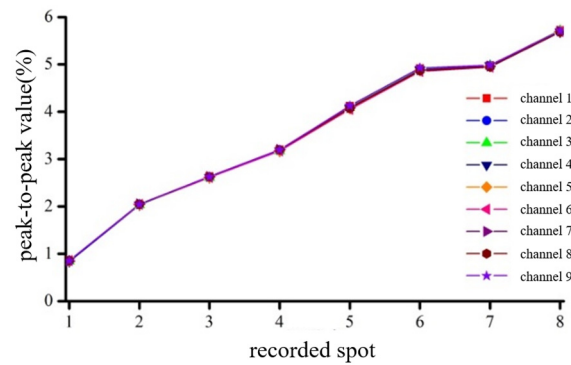

Figure 9. Peak-to-peak value of dynamic point pulsation in each channel of the runner under Optimal Flow Conditions.

The pressure pulsation frequency domain diagram of the eight moving points rv11-rv18 in channel 1 is shown in Figure 10. It can be seen from the diagram that the frequency domain diagram of the eight moving points was similar. From rv11-rv18, the amplitude of 20 times frequency increased gradually, which was due to the fact that the closer the runner was to the outlet, the stronger the RSI of the cascade. This is because near the runner outlet, due to the thrust in the opposite direction of the active guide vane, the flow state is gradually disturbed, and a local backflow area is formed, and this part of the backflow area is reversely offset, resulting in a gradual enhancement of the RSI effect.
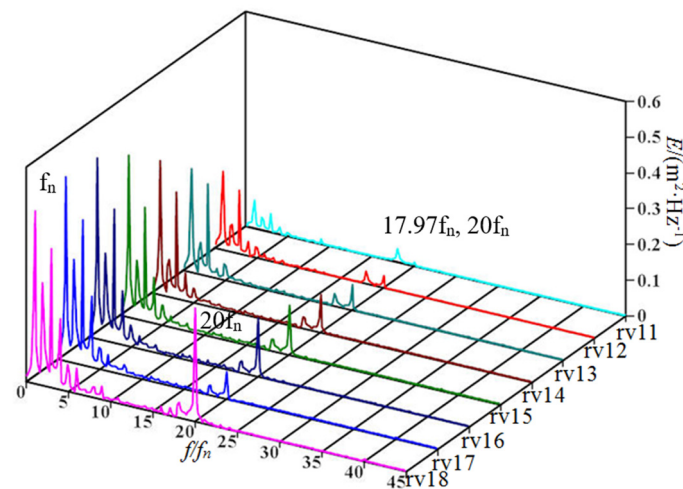

Figure 10. Frequency domain diagram of the pressure fluctuation for the runner channel 1 points.

Then, the pressure pulsation of different static recording points in the whole flow channel was analyzed. After FFT transformation, the frequency domain diagram of the pressure pulsation of each static recording point is shown in Figure 11. It can be seen from the figure that the spectral analysis results of gv1-gv4, mv1-mv4, sv1-sv4, sp1-sp5, and dt11-dt44 were similar. In order to facilitate the analysis, only one point was selected from

the record points with similar results for analysis. In the following, only dt14, gv2, mv2, sv2, and sp2 in the static point were analyzed.
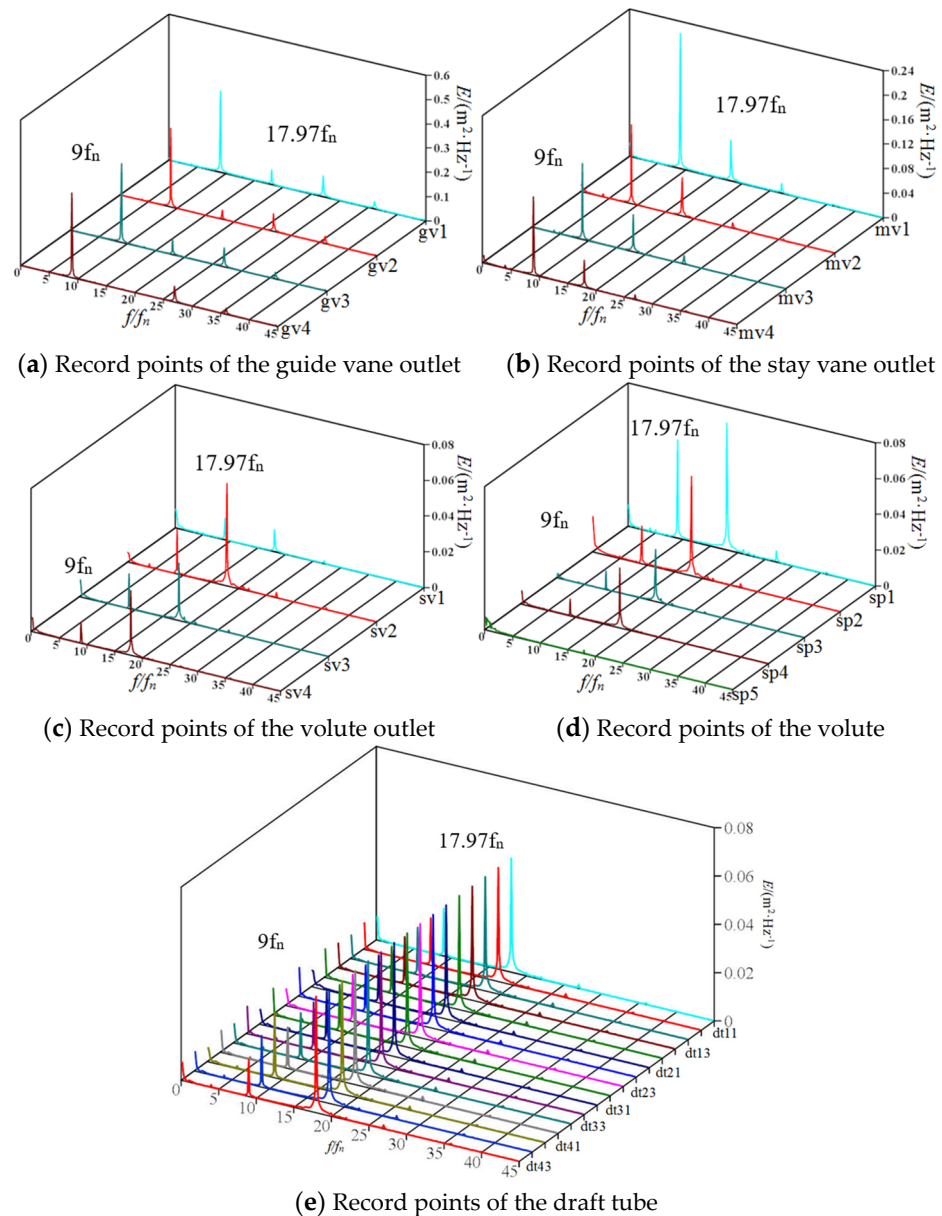

(**a**) Record points of the guide vane outlet

(**b**) Record points of the stay vane outlet

(**c**) Record points of the volute outlet

(**d**) Record points of the volute

(**e**) Record points of the draft tube

Figure 11. Frequency domain diagram of pressure fluctuation at static recording points.

A total of eight recording points were selected to analyze the pressure fluctuation characteristics in the flow components of the pump-turbine. According to the order of water flow, they were dt14, rv11, rv14, rv18, gv2, mv2, sv2, and sp2.

The peak-to-peak values of the eight recording points selected under the optimal conditions are shown in Figure 12, and the curve was an inverted 'V' shape. Among the eight recording points, the peak-to-peak value of dt14 was the smallest, and the peak-to-peak value increased along the flow direction from dt14 to rv18, which indicates that the RSI effect from dt14 to rv18 was continuously enhanced, and the peak-to-peak value reached the highest point at rv18, which was 6.08%. When far away from the runner basin, the peak-to-peak value from gv2 to sp2 basically showed a gradual downward trend, indicating that the influence of RSI gradually weakened after leaving the runner.
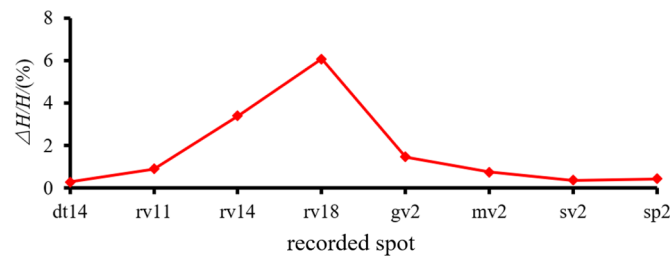
Figure 12. Peak-to-peak pulsation values of the eight recording points in the whole flow channel.

Figure 13 shows the pressure pulsation spectrum analysis of the eight recorded points selected under the optimal working conditions and the change of the amplitude of the relevant pulsation frequency in the flow channel. It can be clearly seen from the diagram that at the point dt14 and the downstream of the runner, the recording points gv2 to sp2, the frequency domain diagram contained the main frequencies $9f_n$, $18f_n$, and $27f_n$, which were nine times the frequency of the rotation frequency, corresponding to the number of blades of the runner. These were the results of the RSI between the runner and the stationary parts, and the pressure pulsation amplitude of $9f_n$ gradually decreased from gv2 to sp2, indicating that it was downstream of the runner basin. The influence of the runner weakened along the direction of water flow.

(**a**) the pressure pulsation frequency domain diagram
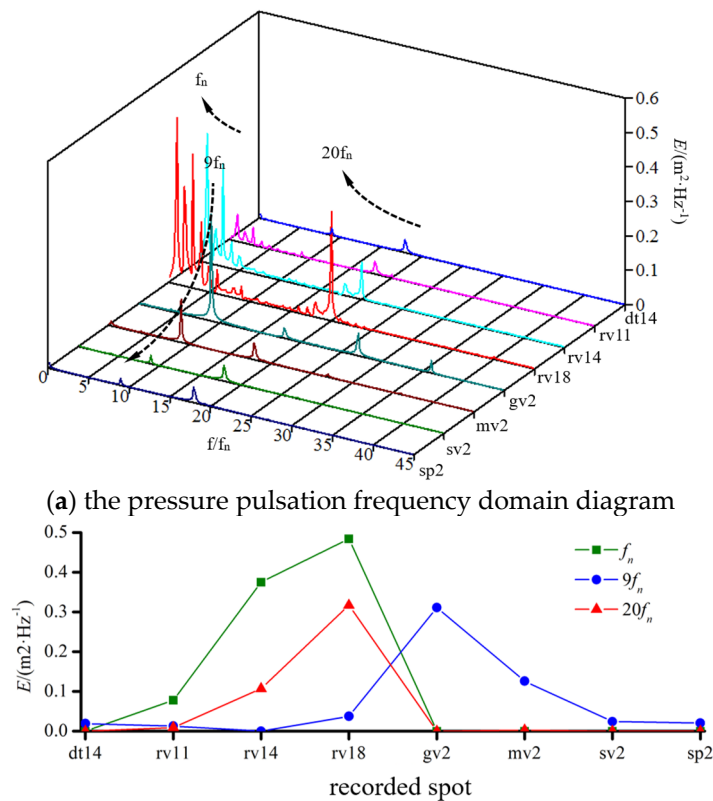
(**b**) the propagation of related frequencies in the flow channel

Figure 13. The pressure pulsation frequency domain diagram of the eight recording points and the propagation of the related frequencies in the flow channel.

For the moving points rv11, rv14, and rv18 inside the runner, the first main frequency was the rotating frequency f_n, and the pressure fluctuation amplitude at the rotating frequency f_n and the rotating frequency doubling nf_n increased from point rv11 to rv18. The amount of $20f_n$ was also included, corresponding to the number of guide vanes, and the pressure fluctuation amplitude increased from rv11 to rv18, indicating that the cascade

played an increasingly more important role along the flow direction in the flow channel. Under the optimal conditions, no low frequency was found, indicating that the flow was relatively smooth under the optimal conditions, as shown in Figure 14.
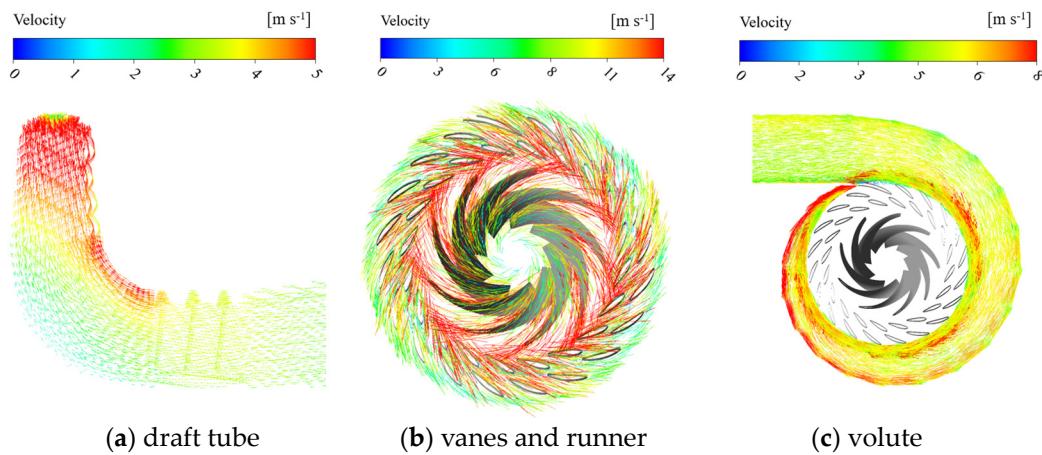

(**a**) draft tube   (**b**) vanes and runner   (**c**) volute

Figure 14. Flow characteristics of the flow components.

5.3. Pressure Pulsation Characteristics under Partial Load Conditions

The partial load condition was 190 L/s (189.4 kg/s, $0.46Q_d$). Under the condition of partial load rate, the mixing amplitude of 72 moving points in 9 channels in the runner domain was analyzed, as shown in Figure 15. It can be found that the distribution of peak-to-peak values in the nine blade channels was further uneven compared with the optimal flow condition, which further indicates that when the operating condition was farther away from the optimal operating condition, the flow in each channel of the runner became more uneven. In order to simplify the analysis, only 16 recording points of channel 1 and channel 5 with the largest difference are analyzed here.
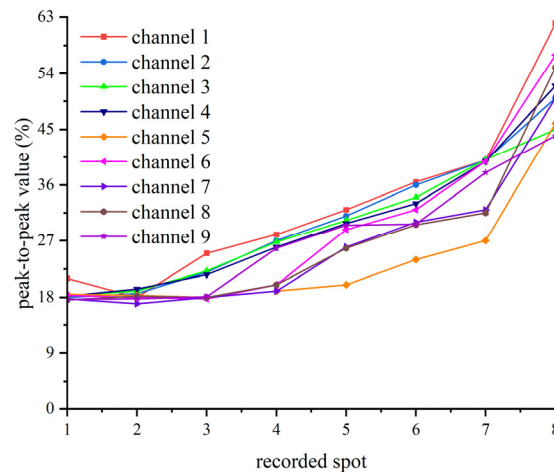

Figure 15. Peak-to-peak value of dynamic point pulsation in each channel of the runner under Partial Load Conditions.

Under the condition of partial load rate, FFT changes were performed on 16 moving points in channel 1 and channel 5 in the runner domain, and the frequency domain diagram of pressure fluctuation was obtained, as shown in Figure 16. It can be found that there were differences in low-frequency values at some corresponding points, indicating that there were differences in the flow of channel 1 and channel 5, resulting in differences in low-frequency values. It is further proven that as the operating conditions were farther and

farther away from the optimal conditions, the flow in each channel of the runner became more uneven.
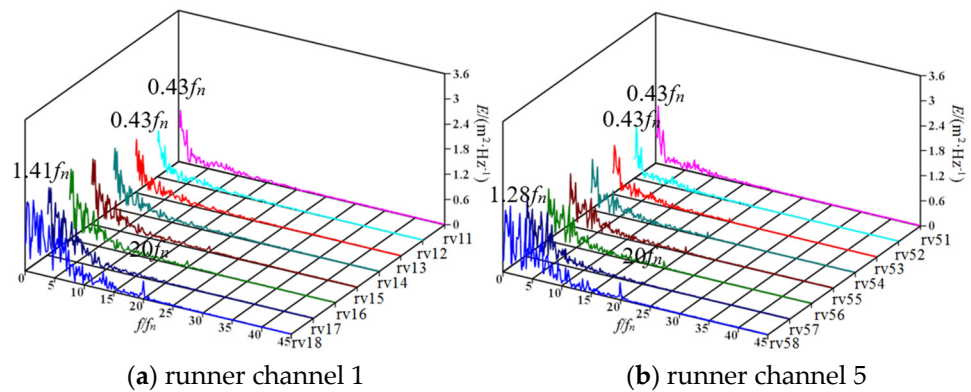

(**a**) runner channel 1   (**b**) runner channel 5

Figure 16. Frequency spectrum analysis of rotating points in runner channel 1 and runner channel 5.

The peak-to-peak values of the eight recording points dt14, rv11, rv14, rv18, gv2, mv2, and sp2 under the low flow condition are shown in Figure 17, and the peak-to-peak value under the low flow condition was increased relative to the optimal flow condition. In summary, as the flow rate decreased, the peak-to-peak value of the same recording point increased continuously, and the larger peak-to-peak value often corresponded to larger flow loss and more complex internal flow conditions.
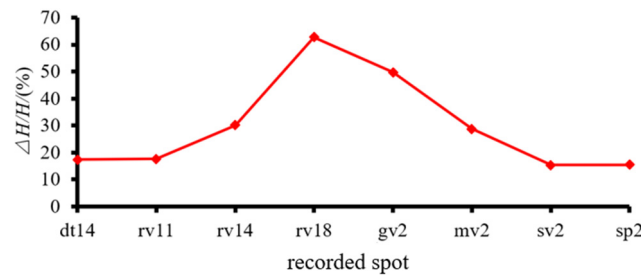

Figure 17. Peak-to-peak values of the eight recording points.

It can also be found from Figure 17 that from dt14 to rv18, the peak-to-peak value increased continuously with the continuous strengthening of the RSI. At rv18, the peak-to-peak value reached the maximum value of 62.78%. When the water flow left the runner, the peak-to-peak value from rv18 to sv2 decreased rapidly, while the peak-to-peak values of sp2 and sv2 were relatively close.

Figure 18 shows the flow characteristics and vortex distribution of each flow component at a low flow rate. It can be seen that after the flow rate decreased, the flow situation in the flow parts became extremely unstable, especially in the straight cone section of the draft tube, resulting in a large number of vortices and serious flow loss.

The FFT transform was performed on the pressure pulsation of the eight recording points at the lowest flow condition point. And the results are shown in Figure 19. At partial load rates, the dominant frequency of the entire basin was more complicated. From point dt14 to point gv2, the dominant frequency was $0.35 f_n$. For point rv18, the first dominant frequency was $1.41 f_n$, and the second dominant frequency was $0.35 f_n$. From point mv2 to sp2, the dominant frequency became the low frequency $0.53 f_n$, and the frequency $9 n f_n$ was completely submerged in a large number of dominant frequency pulsations.
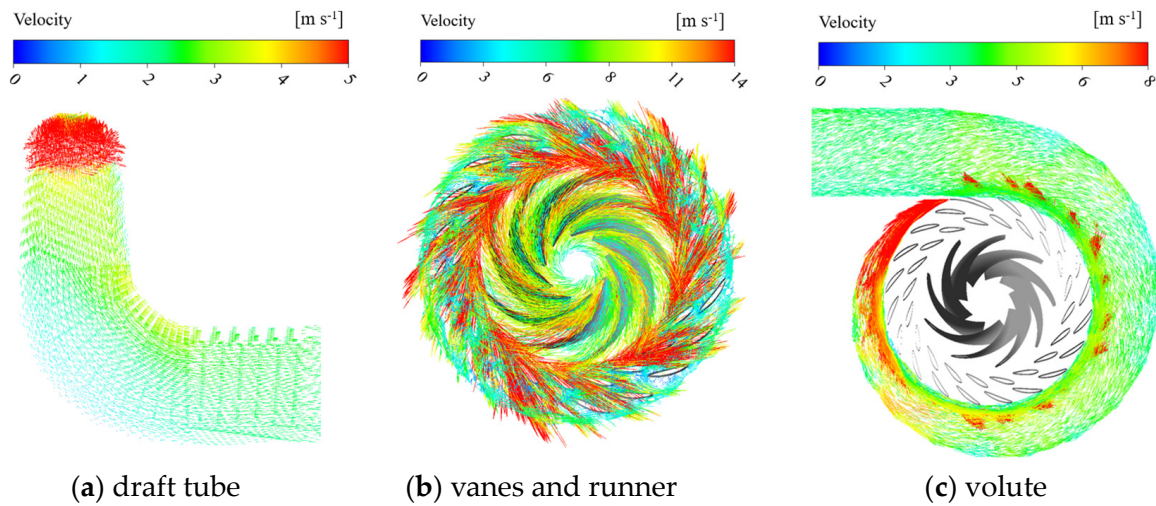
(**a**) draft tube   (**b**) vanes and runner   (**c**) volute

Figure 18. Flow situation of each component.

(**a**) the pressure fluctuation frequency domain diagram

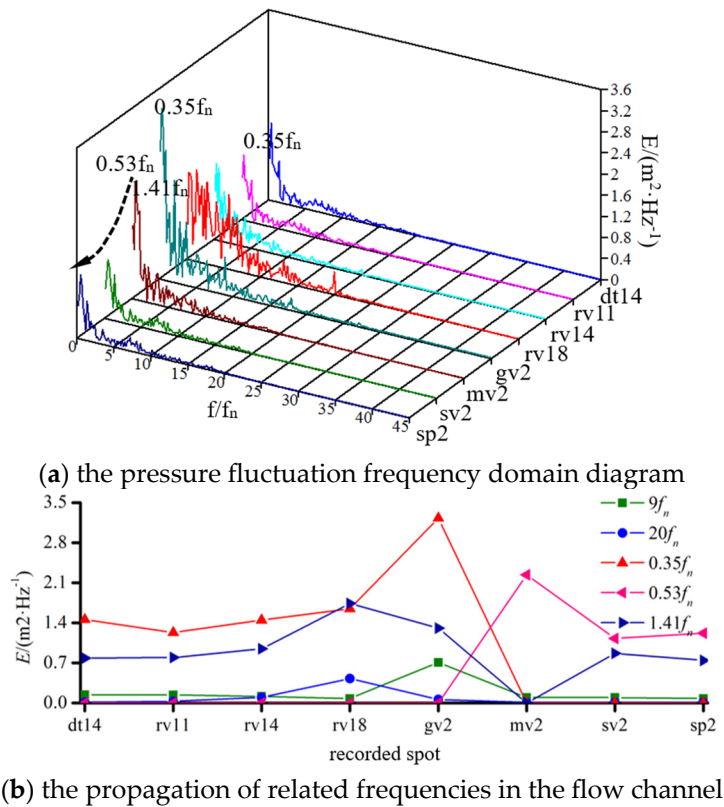(**b**) the propagation of related frequencies in the flow channel

Figure 19. The pressure fluctuation frequency domain diagram of eight recording points and the propagation of related frequencies in the flow channel.

6. Conclusions

(1) Under the condition of the pump, as the flow rate decreased, the increase in head was insufficient to compensate for the hydraulic losses. At this point, the slope of the flow-head curve steepened, and in some cases, a local positive slope appeared, resulting in the formation of a hump area. Under the optimal flow condition, the peak-to-peak value of the draft tube in the hump area was the smallest, and the peak-to-peak value increased along the flow direction. The RSI effect was continuously enhanced, and the peak-to-peak value reached the highest point at the runner. When away from the runner basin, due to

the influence of RSI, the peak-to-peak value from the guide vane to the volute gradually decreased after leaving the rotating runner.

(2) Under the optimal flow condition, no low frequency was found, indicating that the water flow was relatively smooth. The main frequency in the draft tube and the downstream basin of the runner was nine times of the rotating frequency, corresponding to the number of blades of the runner, which is the result of the RSI between the runner and the static components. The amplitude of pressure fluctuation along the flow direction in the runner increased continuously, and the 20 times frequency of the rotation frequency appeared, which was the result of the action of the guide vane cascade.

(3) The peak-to-peak value under partial load conditions was increased relative to the optimal flow conditions. The distribution of peak-to-peak values in the nine runner channels was further uneven compared with the optimal flow condition, indicating that the flow in each runner channel was more uneven when the operating condition was farther away from the optimal operating condition. The peak-to-peak value from the guide vane to the runner increased, which was the result of the continuous strengthening of the RSI.

(4) Under the condition of partial load rate, the main frequency of the whole basin was more complex, and the frequency $9f_n$ was completely submerged in a large number of main frequency pulsations, which indicates that the flow was extremely unstable under the condition of the partial load rate, resulting in the hump area during the operation of the unit.

Author Contributions: Conceptualization, K.Z.; data curation, Z.H.; formal analysis, Y.X.; software, L.C.; supervision, S.R.; writing—original draft, W.X.; visualization, A.K.R.; writing—review and editing, G.S. All authors have read and agreed to the published version of the manuscript.

Data Availability Statement: Data are contained within the article.

Conflicts of Interest: Author K.Z. was employed by the company State Grid Xinyuan Group Co., Ltd.; W.X. was employed by the company Pumped-Storage Technological & Economic Research Institute State Grid Xinyuan Company Ltd. The remaining authors declare that the research was conducted in the absence of any commercial or financial relationships that could be construed as a potential conflict of interest.

References

1. Binama, M.; Kan, K.; Chen, H.-X.; Zheng, Y.; Zhou, D.; Su, W.-T.; Muhirwa, A.; Ntayomba, J. Flow Instability Transferability Characteristics within a Reversible Pump Turbine (RPT) under Large Guide Vane Opening (GVO). *Renew. Energy* **2021**, *179*, 285–307. [CrossRef]
2. Schill, W.-P.; Zerrahn, A. Long-Run Power Storage Requirements for High Shares of Renewables: Results and Sensitivities. *Renew. Sustain. Energy Rev.* **2018**, *83*, 156–171. [CrossRef]
3. Schmidt, J.; Kemmetmüller, W.; Kugi, A. Modeling and Static Optimization of a Variable Speed Pumped Storage Power Plant. *Renew. Energy* **2017**, *111*, 38–51. [CrossRef]
4. Tao, R.; Xiao, R.; Wang, F.; Liu, W. Cavitation Behavior Study in the Pump Mode of a Reversible Pump-Turbine. *Renew. Energy* **2018**, *125*, 655–667. [CrossRef]
5. Shi, G.; Hao, Z.; Peng, X.; Wen, H.; Lv, W.; Fu, J. Analysis of Vortex Characteristics in the S-Shaped Region of a Reversible Pump-Turbine with Different Guide Vane Openings Based on Omega Vortex Identification Method. *J. Energy Storage* **2024**, *84*, 110921. [CrossRef]
6. Nasir, J.; Javed, A.; Ali, M.; Ullah, K.; Kazmi, S.A.A. Capacity Optimization of Pumped Storage Hydropower and Its Impact on an Integrated Conventional Hydropower Plant Operation. *Appl. Energy* **2022**, *323*, 119561. [CrossRef]
7. Sawle, Y.; Gupta, S.C.; Bohre, A.K. Review of Hybrid Renewable Energy Systems with Comparative Analysis of Off-Grid Hybrid System. *Renew. Sustain. Energy Rev.* **2018**, *81*, 2217–2235. [CrossRef]
8. Tao, R.; Song, X.; Ye, C. Pumped Storage Technology, Reversible Pump Turbines and Their Importance in Power Grids. *Water* **2022**, *14*, 3569. [CrossRef]
9. Zuo, Z.; Fan, H.; Liu, S.; Wu, Y. S-Shaped Characteristics on the Performance Curves of Pump-Turbines in Turbine Mode—A Review. *Renew. Sustain. Energy Rev.* **2016**, *60*, 836–851. [CrossRef]
10. Olimstad, G.; Nielsen, T.; Børresen, B. Dependency on Runner Geometry for Reversible-Pump Turbine Characteristics in Turbine Mode of Operation. *J. Fluids Eng.* **2012**, *134*, 121102. [CrossRef]

11. Cavazzini, G.; Houdeline, J.-B.; Pavesi, G.; Teller, O.; Ardizzon, G. Unstable Behaviour of Pump-Turbines and Its Effects on Power Regulation Capacity of Pumped-Hydro Energy Storage Plants. *Renew. Sustain. Energy Rev.* **2018**, *94*, 399–409. [CrossRef]

12. Zhang, W.; Chen, Z.; Zhu, B.; Zhang, F. Pressure Fluctuation and Flow Instability in S-Shaped Region of a Reversible Pump-Turbine. *Renew. Energy* **2020**, *154*, 826–840. [CrossRef]

13. Pang, S.; Zhu, B.; Shen, Y.; Chen, Z. S-Shaped Characteristics of Pump Turbine with Large Guide Vane Opening by Experimental and Numerical Analysis. *AIP Adv.* **2023**, *13*, 015201. [CrossRef]

14. Hu, J.; Zhao, Z.; He, X.; Zeng, W.; Yang, J.; Yang, J. Design Techniques for Improving Energy Performance and S-Shaped Characteristics of a Pump-Turbine with Splitter Blades. *Renew. Energy* **2023**, *212*, 333–349. [CrossRef]

15. Xu, L.; Kan, K.; Zheng, Y.; Liu, D.; Binama, M.; Xu, Z.; Yan, X.; Guo, M.; Chen, H. Rotating Stall Mechanism of Pump-Turbine in Hump Region: An Insight into Vortex Evolution. *Energy* **2024**, *292*, 130579. [CrossRef]

16. Qin, Y.; Li, D.; Zhu, Y.; Wang, H.; Wei, X. Influence of Geometric Factors at Runner Outlet on the Hump Characteristics of a Pump-Turbine. *Sustain. Energy Technol. Assess.* **2022**, *51*, 101890. [CrossRef]

17. Li, D.; Gong, R.; Wang, H.; Xiang, G.; Wei, X.; Qin, D. Entropy Production Analysis for Hump Characteristics of a Pump Turbine Model. *Chin. J. Mech. Eng.* **2016**, *29*, 803–812. [CrossRef]

18. Yang, J.; Pavesi, G.; Yuan, S.; Cavazzini, G.; Ardizzon, G. Experimental Characterization of a Pump–Turbine in Pump Mode at Hump Instability Region. *J. Fluids Eng.* **2015**, *137*, 051109. [CrossRef]

19. Deyou, L.; Hongjie, W.; Gaoming, X.; Ruzhi, G.; Xianzhu, W.; Zhansheng, L. Unsteady Simulation and Analysis for Hump Characteristics of a Pump Turbine Model. *Renew. Energy* **2015**, *77*, 32–42. [CrossRef]

20. Jia, J.; Zhang, J.; Qu, Y.; Cai, H.; Chen, S. Study on Hump Characteristics of Pump Turbine with Different Guide Vane Exit Angles. *IOP Conf. Ser. Earth Environ. Sci.* **2019**, *240*, 072038. [CrossRef]

21. Li, D.; Zhu, Y.; Lin, S.; Gong, R.; Wang, H.; Luo, X. Cavitation Effects on Pressure Fluctuation in Pump-Turbine Hump Region. *J. Energy Storage* **2022**, *47*, 103936. [CrossRef]

22. Li, D.; Song, Y.; Lin, S.; Wang, H.; Qin, Y.; Wei, X. Effect Mechanism of Cavitation on the Hump Characteristic of a Pump-Turbine. *Renew. Energy* **2021**, *167*, 369–383. [CrossRef]

23. Fu, X.; Li, D.; Wang, H.; Zhang, G.; Li, Z.; Wei, X. Influence of the Clearance Flow on the Load Rejection Process in a Pump-Turbine. *Renew. Energy* **2018**, *127*, 310–321. [CrossRef]

24. Qin, Y.; Li, D.; Wang, H.; Liu, Z.; Wei, X.; Wang, X.; Yang, W. Comprehensive Hydraulic Performance Improvement in a Pump-Turbine: An Experimental Investigation. *Energy* **2023**, *284*, 128550. [CrossRef]

25. Hu, D.; Cheng, Y.; Zhang, P.; Wang, X.; Ding, J.; Zhang, X. Distribution Features of Flow Patterns and Pressure Pulsations of Pump-Turbine in Five Operating Modes on the Four-Quadrant Plane. *Front. Energy Res.* **2022**, *10*, 880293. [CrossRef]

26. Ma, Z.; Zhu, B. Pressure Fluctuations in Vaneless Space of Pump-Turbines with Large Blade Lean Runners in the S-Shaped Region. *Renew. Energy* **2020**, *153*, 1283–1295. [CrossRef]

27. Guo, L.; Liu, J.; Wang, L.; Qin, D.; Wei, X. Pressure Fluctuation Propagation of a Pump Turbine at Pump Mode under Low Head Condition. *Sci. China Technol. Sci.* **2014**, *57*, 811–818. [CrossRef]

28. Vagnoni, E.; Andolfatto, L.; Guillaume, R.; Leroy, P.; Avellan, F. Interaction of a Rotating Two-Phase Flow with the Pressure and Torque Stability of a Reversible Pump-Turbine Operating in Condenser Mode. *Int. J. Multiph. Flow* **2019**, *111*, 112–121. [CrossRef]

29. Maruzewski, P.; Hayashi, H.; Munch, C.; Yamaishi, K.; Hashii, T.; Mombelli, H.P.; Sugow, Y.; Avellan, F. Turbulence Modeling for Francis Turbine Water Passages Simulation. *IOP Conf. Ser. Earth Environ. Sci.* **2010**, *12*, 012070. [CrossRef]

30. Li, D.; Qin, Y.; Wang, J.; Zhu, Y.; Wang, H.; Wei, X. Optimization of Blade High-Pressure Edge to Reduce Pressure Fluctuations in Pump-Turbine Hump Region. *Renew. Energy* **2022**, *181*, 24–38. [CrossRef]

31. Li, D.; Wang, H.; Chen, J.; Nielsen, T.; Qin, D.; Wei, X. Hysteresis Characteristic in the Hump Region of a Pump-Turbine Model. *Energies* **2016**, *9*, 620. [CrossRef]

32. Yu, Z.-F.; Yan, Y.; Wang, W.-Q.; Liu, X.-S. Entropy Production Analysis for Vortex Rope of a Francis Turbine Using Hybrid RANS/LES Method. *Int. Commun. Heat Mass Transf.* **2021**, *127*, 10549. [CrossRef]

33. Menter, F.R. Two-equation eddy-viscosity turbulence models for engineering applications. *AIAA J.* **1994**, *32*, 1598–1605. [CrossRef]

34. Hao, Z.; Shi, G.; Peng, X.; Chai, H.; Lv, W.; Huang, Z. Study on the Influence of Vortex Spatial-Temporal Evolution on the Causes of Hump Region of Pump-Turbine and the Characteristics of Vortex Dynamics. *J. Energy Storage* **2024**, *92*, 112297. [CrossRef]